SAN098-0621C

SAND--98-0621C

CONF-980537--

RECEIVED

MAR 17 1998

OSTI

CAD-Driven Microassembly and Visual Servoing

John T. Feddema and Ronald W. Simon[1]
Sandia National Laboratories
P.O. Box 5800, MS 1003
Albuquerque, NM 87185

Abstract

This paper describes current research and development on a robotic visual servoing system for assembly of LIGA (Lithography Galvonoforming Abforming) parts. The workcell consists of an AMTI robot, precision stage, long working distance microscope, and LIGA fabricated tweezers for picking up the parts. Fourier optics methods are used to generate synthetic microscope images from CAD drawings. These synthetic images are used off-line to test image processing routines under varying magnifications and depths of field. They also provide reference image features which are used to visually servo the part to the desired position.

1. Introduction

Over the past decade, considerable research has been performed on Robotic Visual Servoing (RVS) (see [1][2] for review and tutorial). Using real-time visual feedback, researchers have demonstrated that robotic systems can pick up moving parts, insert bolts, apply sealant, and guide vehicles. With the rapid improvements being made in computing, image processing hardware, and CCD cameras, the application of RVS techniques are now becoming widespread.

Ideal applications for RVS are typically those which require extreme precision and cannot be performed cost effectively with fixturing. As the manufacturing lot size of the product increases, it is usually more cost effective to design a set of fixtures to hold the parts in the proper orientations. However, for small lot sizes and large numbers of diverse parts, vision becomes an essential sensor. Historically, computer vision has been used in a look-and-move mode where the vision system first locates the part in robot world coordinates, and then the robot moves "blindly" to that location and picks up the part. In the 1980s, computing and image processing hardware improved to the point where vision can now be used as a continual feedback sensor for controlling the relative position between the robot and the part. RVS is inherently more precise than look-and-move vision because an RVS error-driven control law improves the relative positioning accuracy even in the presence of modeling (robot, camera, or object) uncertainties.

One ideal application for RVS which meets these requirements is the microassembly of MEMS (Micro-ElectroMechanical Systems) components. In recent years, the world economy has seen expansive market growth in the area of MEMS. It is predicted that the MEMS market could reach more than $34 billion by the year 2002. Today, commercially available MEMS products include inkjet printer heads and accelerometers for airbags. These products require little or no assembly because a monolithic integrated circuit process is used to develop the devices. However, future MEMS products may not be so fortunate. Monolithic integration is not feasible when incompatible processes, complex geometry, or different materials are involved. For these cases, new and extremely precise micromanipulation capabilities will be required for successful product realization.

Sandia National Laboratories is currently developing manufacturing processes to make MEMS parts with 10-100 micron outer dimensions and submicron tolerance for use in weapons surety devices. In particular, Sandia is pursuing both surface machined silicon and LIGA (Lithography Galvonoforming Abforming) parts. The surface machined silicon devices are fabricated in place using several layers of etched silicon and generally do not require assembly. However, the LIGA parts are batch fabricated and do require assembly. The LIGA parts are formed by using X-ray lithography to create molds in PMMA (polymethylmethacrylate) and then electroplating metals (typically nickel, permalloy, and copper) in the molds. Afterwards, the metal parts are released into Petrie dishes. LIGA parts are of special interest because they can be made thicker than silicon parts (hundreds of microns verses tens of microns), they can be made of metals which makes them stronger in tension than surface machined silicon, and they can contain iron which allows them to be configured as miniature electromagnetic motors. The disadvantage of LIGA parts over silicon

---

1

MASTER

1998042O 027

structures is that they must be assembled. The required precision, operator stress and eye strain associated with assembling such minute parts under a microscope generally precludes manual assembly from being a viable option. An automated assembly system addresses these problems.

There are several reasons why RVS is ideally suited for the assembly of LIGA parts. First, from a physiological stand point, human beings exclusively use their vision sense to assemble parts this size. People do not use force feedback because they can not feel micro-Newtons of force. Second, since the LIGA parts are randomly placed in dishes and it is difficult to design parts feeders and fixturing with submicron tolerances, vision is required to locate the parts. Third, the environment under a microscope is structured and the parts are well known. Fourth, most assembly operations are 4 degrees of freedom (DOF) problems (x, y, z, and rotation about z). These last two points greatly simplify the image processing required to recognize and locate the parts.

In addition to the above points, this problem is well suited for a completely automated manufacturing process based on CAD information. The LIGA parts are originally designed using CAD packages such as AutoCAD, ProE, or Velum. The designs are then translated to GDSII, which is the format that the mask shops use to develop the X-ray masks for the LIGA process. Therefore, we already have CAD information on each part. Also, since X-rays are used to develop the LIGA molds, both the horizontal and vertical tolerances of the parts are quite precise (submicron horizontal tolerances, and 0.1 micron taper over 100 microns of thickness). Therefore, there is excellent correspondence between the CAD model and the actual part.

If a synthetic microscope image of the part could be created, it would solve one very important RVS issue: where do the image reference features come from? The reference features could be learned through teach-by-showing of actual parts, however, this is not cost effective in an agile manufacturing environment. Instead, it would be best if the reference image features could be derived directly from the CAD model. In this way, the model could be used for assembly planning even before the parts are produced.

Even with an accurate CAD model, there are several issues that cause microassembly to be a difficult assembly planning problem. As discussed by others in the field [3][4], the relative importance of the interactive forces in microassembly is very different from that in the macro world. Gravity is almost negligible, while surface adhesion and electrostatic forces dominate. To some extent these problems can be reduced by clean parts and grounding surfaces. But the assembly plan should take these effects into account.

To date, several different approaches to teleoperated micromanipulation have been attempted. Miyazaki [5] and Kayono [6] meticulously picked up 35 polymer particles (each 2 microns in diameter) and stacked them inside of a scanning electron microscope (SEM). Mitsuishi [7] developed a teleoperated, force-reflecting, micromachining system under a SEM. On a larger scale, Zesch [8] used a vacuum gripper to pick up 100 micron size diamond crystals and deposit them to arbitrary locations. Sulzmann [9] teleoperated a microrobot using 3D computer graphics (virtual reality) as the user interface.

More recently, researchers have gone beyond teleoperation to use visual feedback to automatically guide microrobotic systems. Sulzmann [9] illuminated gallium phosphate patches on a microgripper with an ion beam, and he used the illuminated features to locate and position the microgripper. Vikramaditya [10] investigated using visual servoing and depth-from-defocus to bring parts into focus and to a specified position in the image plane. The estimation of depth from focus has also been addressed by several other researchers [11-14].

In this paper, we take the next step by creating synthetic images from CAD data. These images are used to test image processing algorithms off-line and to create reference image features which are used on-line for visual servoing. The next four sections describe the workcell, an optics model used to generate synthetic images, resolved rate visual servoing equations, as well as ongoing CAD-Driven assembly planning work.

2. Workcell Description

Our microassembly workcell consists of a 4 DOF AMTI (subsidiary of ESEC) Cartesian assembly system, a 4 DOF precision stage, micro-tweezers, and a long working distance microscope (see Figure 1). The AMTI robot has a repeatability of 0.4 microns in the x and y directions, 8 microns in the z direction, and 23.56 arc-seconds in rotation about z. The precision stage has a repeatability of approximately 1 micron in x, y, and z, and 1.8 arc-seconds in rotation about z. The microscope is fixed above the stage and has an motor-driven zoom and focus.

DISCLAIMER

Figure 1. Microassembly Workcell.
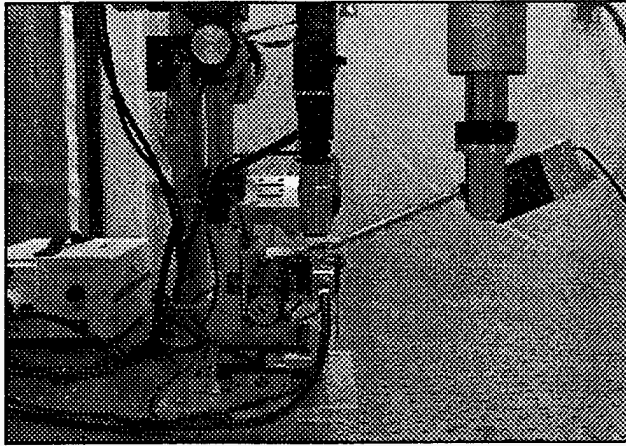

Figure 2. LIGA tweezers placing a LIGA gear on a 44 micron OD shaft.

During assembly operations, the AMTI robot positions the micro-tweezers above the stage and within the field of view of the microscope. The precision stage is used to move the LIGA parts between the fingers of the tweezers. The tweezers are closed on the first part, the stage is lowered, and the mating part on the stage is brought into the field of view. The stage is then raised into position and the part in the tweezers is released.

The micro-tweezers is a LIGA fabricated tweezers [15] which is actuated by a linear ball-and-screw DC motor and a collet style closing mechanism. The current version of these tweezers is 20.8 mm long, 200 microns thick, and has two fingers which are 100 microns wide.

A teleoperated interface was developed to test simple pick-and-place operations. The AMTI robot, the 4 DOF precision stage, the micro-tweezers, and the focus, magnification, and lighting of the microscope are controlled through a custom developed user interface built within an Adept A-series VME controller. The image of the parts as seen by the microscope is displayed on the computer screen. The x and y position of the robot and stage are controlled by the operator by dragging a cursor on the graphical display. Sliders are used to control the z position and theta orientation of the robot and stage as well as the microscope focus, magnification, and lighting.

This teleoperated interface has been used to pick up and place 100 micron O.D. LIGA gears with 50 micron holes on pins ranging from 35 to 49 microns (see Figure 2). The next step is to automate the assembly using visual feedback. The next section describes the optical model used to evaluate the microscope's depth of field and generate synthetic images from CAD data.
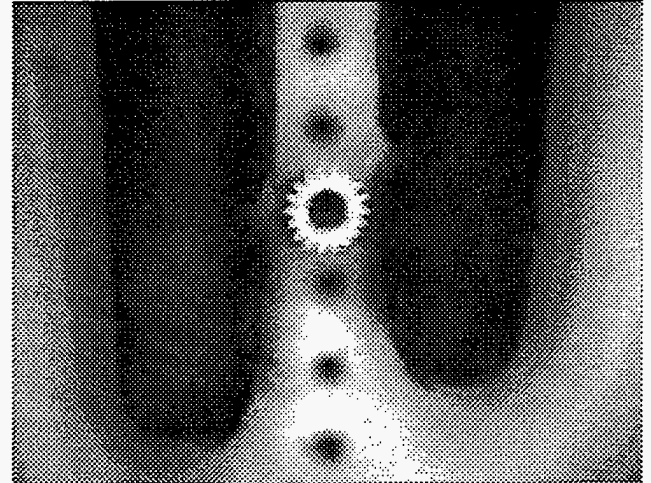
3. Optics Modeling

When viewing parts on the order of 100 microns in dimension, it is important to have a precise model of the optics, including models of the field of view and depth of field. This model is even more important if the assembly is to be performed automatically from CAD information. What is needed is a way to create a synthetic image before the part is even produced. Then we can design for assembly and determine off-line the required image processing routines for assembly. In this regard, Fourier optics methods can be used to create synthetic images from the CAD drawings.

First, we provide a simple review of microscope optics. In our experiments, we are using a long working distance microscope by Navitar. This microscope uses an infinity-focused objective lens. Referring to Figure 3, the rays emanating from a given objective point are parallel between the objective and the tube lens. The tube lens is used to focus the parallel rays onto the image plane. The magnification is calculated by dividing a focal length of the tube lens by the focal length of the objective lens [16].
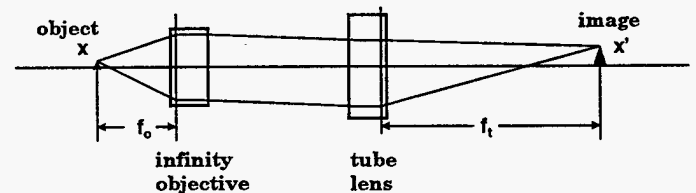

Figure 3. Infinity corrected microscope optics.

$$x' = mx \quad \text{and} \quad y' = my \quad \text{where} \quad m = \frac{f_t}{f_o}, \quad (1)$$

(x, y) is the object position in the objective focal plane, (x', y') is the projected position in the image plane, m is the lateral magnification, f_t is the focal length of the tube lens, and f_o is the focal length of the objective. With our microscope, the focal length of the tube lens is adjustable so that the magnification varies from 6.9 to 44.5.
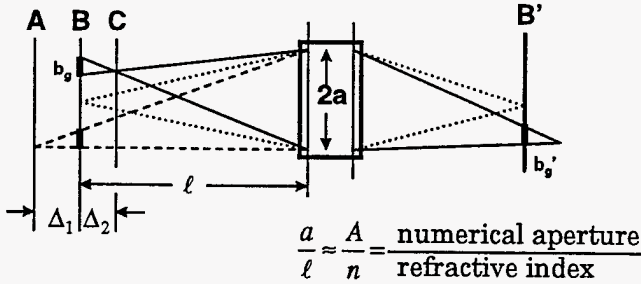

$$\frac{a}{\ell} \approx \frac{A}{n} = \frac{\text{numerical aperture}}{\text{refractive index}}$$

Figure 4. Geometric depth of field.

The depth of field can be determined by analyzing Figure 4. Here, the objective and tube lens are modeled as a single thick lens with magnification m. The in-focus object plane is denoted as **B**, and the corresponding in-focus image plane is denoted as **B'**. When the object is moved out of focus to planes **A** or **C**, a point on **A** or **C** is projected into a disk of diameter b_g on object plane **B**. The resulting disk in the image plane has diameter b_g'.

By using similar triangles, the geometric depth of field is given by

$$\Delta_g = \Delta_1 + \Delta_2 \approx \frac{n b_g'}{mA} \quad (2)$$

where n is the refractive index of the optics, and A is the numerical aperture of the optics [17]. This expression is valid if object blur b_g on plane B is much less than the lens aperture radius a. Solving this equation for the defocused blur in the image,

$$b_g' = \frac{2mA|\Delta|}{n} \quad (3)$$

where $\Delta = \Delta_1 \approx \Delta_2$.

In addition to the geometric depth of field, Fraunhofer diffraction is also important as the objects being viewed approach the wavelength of light. Rayleigh's Criteria [18] says that the diameter of the Airy disk in the image plane is

$$b_r' = \frac{1.22\lambda m}{A} \quad (4)$$

where λ is the wavelength of incident light. This is the diameter of the first zero crossing in an intensity image of a point source when viewed through an ideal circular lens with numerical aperture A and magnification m.

Assuming linear optics, the geometric blur diameter and the Airy disk diameter are additive. Adding Equations (3) and (4) and solving for Δ, the total depth of field is given by:

$$\Delta_T = 2\Delta = \frac{nb'}{mA} - \frac{1.22\lambda n}{A^2} \quad (5)$$

where $b' = b_g' + b_r'$ is the acceptable blur in the image.

The first term is due to geometric optics, while the second term is due to diffraction from Rayleigh's criteria. Since Equation (5) must always be positive, the acceptable geometric blur must be larger than the Airy disk. Note that even when the object is in perfect focus ($\Delta_T = 0$), there is still a small amount of blurring due to diffraction. For example, the parameters for the microscope used in the experiments are $n=1.5$, $\lambda=0.6$ microns, $A=0.42$, and $m=6.9$. The resulting image blur due to diffraction (Airy disk diameter) is 12.026 microns. If the acceptable image blur is 12.45 microns (approximately 1 pixel on a 1/3 inch format CCD), then $\Delta_T = 0.22$ microns. Therefore, two points separated by b'/m or 1.8 microns will become indistinguishable if the points are moved as little as 0.11 microns out of the focal plane!

The next problem is how to generate synthetic images which account for the geometric depth of field and the Fraunhofer diffraction. Using Fourier optics [18], a stationary linear optical system with incoherent lighting is described in terms of a 2D convolution integral:

$$I_{im}(x', y') = \iint I_{obj}(x, y)S(x - x', y - y')dxdy \quad (6)$$

where $I_{im}(x', y')$ is the image intensity, $I_{obj}(x, y)$ is the object intensity, and $S(x,y)$ is the impulse response or point spread function. This convolution is more efficiently computed using Fourier Transforms:

$$\tilde{I}_{im}(u,v) = \tilde{I}_{obj}(u,v)\tilde{S}(u,v) \quad (7)$$

where the tilde represents the 2D Fourier Transform of the function, and u and v are spatial frequencies in the x and y directions.

Considering only the geometric depth of field, the impulse response is

$$S_g(r', \theta') = \begin{cases} \dfrac{4}{\pi(b_g')^2} & r' \leq b_g'/2 \\ 0 & r' > b_g'/2 \end{cases} \quad (8)$$

where r' is the radial distance for the impulse location in the image plane. The impulse response is radial symmetric about the impulse location and independent of θ'. This implies that a geometrically defocused image is the focused image convolved with a filled circle of diameter b_g'.

Considering only Fraunhoffer diffraction, the impulse response is

$$S_d(r',\theta') = \pi^2 a^4 \left| \frac{2 J_1\left(\frac{2\pi a r'}{\lambda f m}\right)}{\frac{2\pi a r'}{\lambda f m}} \right|^2 \qquad (9)$$

where $J_1(\bullet)$ is the first order Bessel function, a is the aperture radius, λ is the wavelength of light, and f is the focal length of the lens. This function is also radial symmetric about the impulse location and independent of θ'. In addition, it is the expression used to generate the Airy disk. It would be computationally expensive to convolve this expression with the original image without the use of Fourier Transforms. Fortunately, there exists a simple expression in the Fourier domain. With incoherent light, the Fourier Transform of the impulse response is given by the autocorrelation of the aperture (pupil) function with its complex conjugate:

$$\tilde{S}_d(u,v) = \iint P^*(x,y)P(x+\lambda z'u, y+\lambda z'v)dxdy \qquad (10)$$

For a circular aperture of radius a, the pupil function is

$$P(r_{uv},\theta) = \begin{cases} 1 & r_{uv} \leq a \\ 0 & r_{uv} > a \end{cases} \qquad (11)$$

and the resulting transfer function is given by

$$\tilde{S}_d(r_{uv}) = 2a\left[a\sin^{-1}\left(\sqrt{1-\left(\frac{r_{uv}}{2a}\right)^2}\right) - \frac{r_{uv}}{2}\sqrt{1-\left(\frac{r_{uv}}{2a}\right)^2} \right]$$
$$(12)$$

where r_{uv} is the radius in image frequency.

The combined impulse response of both the geometric depth of field and the Fraunhoffer diffraction is given by the convolution of S_g and S_d, or in the frequency domain, the product of $\tilde{S}_g$ and $\tilde{S}_d$. It should be noted that both S_g and S_d act as low pass filters on the image. S_g becomes the more dominant filter as the object is moved out of the focal plane. A block diagram of the entire synthetic image generation process is given in Figure 5.
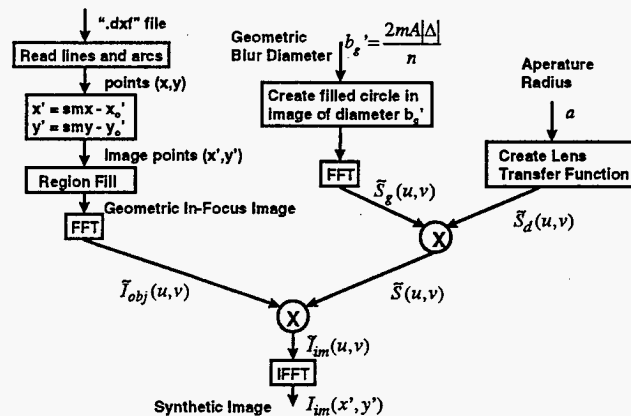

Figure 5. Block Diagram of synthetic image generation.

Synthetically generated examples of Fraunhoffer diffraction and geometric blur are shown in Figures 6-8. Figure 6 shows the geometric and out-of-focus images of a 100 micron gear. Figure 7 shows a cross section of the geometric image and the same image after Fraunhoffer diffraction. Notice how the edges of the gear are rounded. Figures 8 shows a cross section of the image which is out-of-focus. The geometric blur becomes the dominant effect as the out-of-focus distance increases.
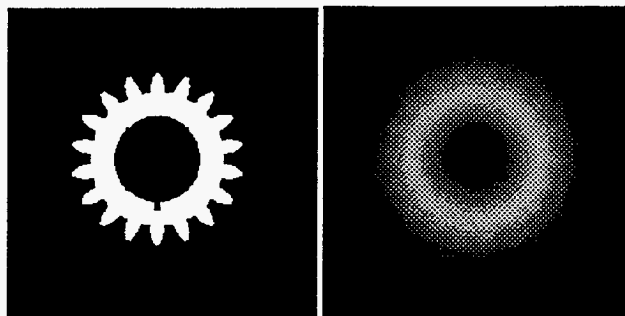

Figure 6. Synthetically generated images. The image on the left is in-focus. The image on the right is a diffracted image which is 25 microns out of depth of field.
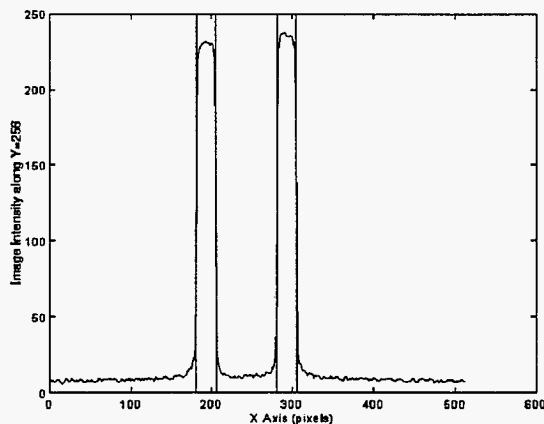

Figure 7. Cross section of geometric in-focus image (vertical lines) and diffracted in-focus image.
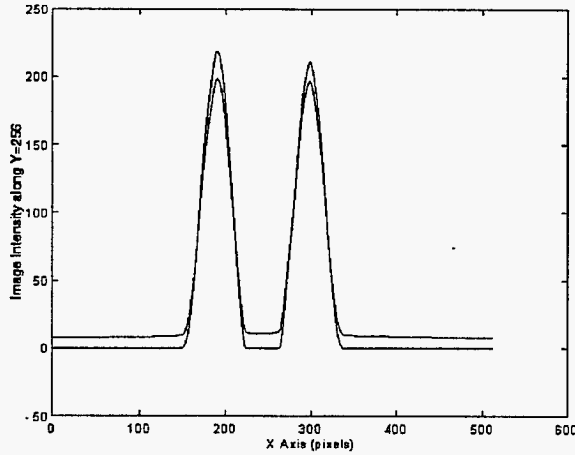
5

Figure 8. Cross section of a diffracted image which is 25 microns out of depth of field. The cross section due only to geometric blurring is the curve which starts at zero and has peaks at 225. When diffraction is included, the image does not start at zero and the peaks are attenuated.

These results can be compared to real images of a 100 micron gear under a microscope as shown in Figures 9 and 10. Figure 9 shows an image of the gear when in-focus, and when moved out-of-focus by 30 microns. Figure 10 shows a cross section of the in-focus and out-of-focus images. Notice that the edges of the in-focus image are rounded. Also, notice that the intensity of the out-of-focus image is attenuated and the slope is more gradual than the in-focus image. These results were predicted by the synthetic image (see Figures 6-8). However, the comparison also highlights some effects which are not yet modeled. In particular, the through-the-lens lighting is not uniform, and there are shadowing effects inside the gear. Also, the above analysis is only valid for parts which are all in the same z plane. Nevertheless, we can use this synthetic image to derive reference features for visual servoing, as will be shown next.
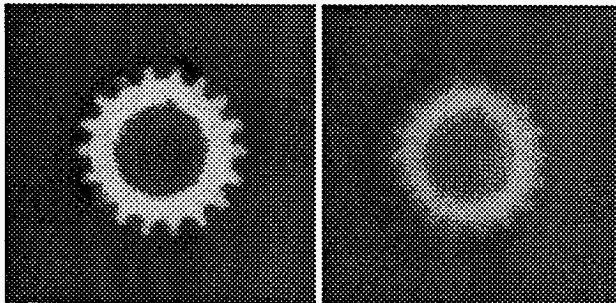

Figure 9. Real experimental images. The image on the left is in focus. The image on the right is an image which is 30 microns out of depth of field.
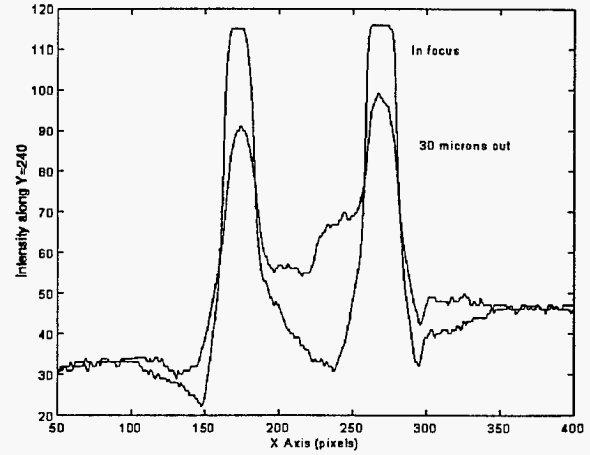

Figure 10. Cross section of in-focus and out-of-focus images in Figure 9.

4. Visual Servoing

As pointed out in [2], there are two ways in which to perform visual servoing: position-based and image-based. We are using the image-based approach. In this approach, the inverse image Jacobian is need to transform the differential motion in image coordinates into differential motion in the camera coordinates. The differential motion in the camera coordinates is, in turn, transformed to either robot end-effector or stage coordinates via another constant Jacobian relationship.

Since we are only interested in 4 DOF motion, the forward Jacobian of a single image point is a 2x4 matrix. Differentiating Equation (1) and inserting the linear and angular velocities with respect to the camera frame, the image Jacobian relationship for a single image feature point is

$$\begin{bmatrix} \dot{x}' \\ \dot{y}' \end{bmatrix} = \begin{bmatrix} m & 0 & 0 & -y' \\ 0 & m & 0 & -x' \end{bmatrix} \begin{bmatrix} {}^c\dot{x} \\ {}^c\dot{y} \\ {}^c\dot{z} \\ {}^c\omega_z \end{bmatrix} \quad (13)$$

where $(\dot{x}', \dot{y}')$ is the velocity of the projected point in the image plane, $\left({}^c\dot{x}, {}^c\dot{y}, {}^c\dot{z}\right)$ is the linear velocity of the actual point with respect to the camera coordinate frame, and ${}^c\omega_z$ is the rotational velocity of the actual point about the z axis of the camera coordinate frame. Notice that in this expression, the linear motion along the optical axis z can not be observed. However, we know from the previous section that motion along the optical axis can be observed from the blurred diameter of a point. Summing and differentiating the expressions for blur diameter in

6

Equations (3) and (4) and combining the result with Equation (13), an augmented image Jacobian for a single point can be defined as

$$\begin{bmatrix} \dot{x}' \\ \dot{y}' \\ \dot{b}' \end{bmatrix} = \begin{bmatrix} m & 0 & 0 & -y' \\ 0 & m & 0 & -x' \\ 0 & 0 & \dfrac{2mA}{n} & 0 \end{bmatrix} \begin{bmatrix} {}^c\dot{x} \\ {}^c\dot{y} \\ {}^c\dot{z} \\ {}^c\omega_z \end{bmatrix}. \qquad (14)$$

where $\dot{b}'$ is the differential change in blur in the image plane. Since the motion along z is independent of the other degrees of freedom, we can solve for that separately.

$$\left| {}^c\dot{z} \right| = \frac{n}{2mA}\dot{b}' \qquad (15)$$

One simple way to realize Equation (15) and bring the parts into focus is to take the gradient of successive images and move the part along the z axis until the sum of gradient values in the image is maximized. This gradient maximum occurs when the blur is a minimum and the edges are sharp. This focusing process is essentially what camcorders do to automatically adjust their depth of focus.

To control orientation, two image points must be observed. The inverse least squares solution to Equation (13) is

$$\begin{bmatrix} {}^c\dot{x} \\ {}^c\dot{y} \\ {}^c\omega_z \end{bmatrix} = \left(J^T J\right)^{-1} J^T \begin{bmatrix} \dot{x}_1' \\ \dot{y}_1' \\ \dot{x}_2' \\ \dot{y}_2' \end{bmatrix} \quad \text{where} \quad J = \begin{bmatrix} m & 0 & -y_1' \\ 0 & m & -x_1' \\ m & 0 & -y_2' \\ 0 & m & -x_2' \end{bmatrix}$$
$$(16)$$

The subscripts of x and y denote either point 1 or 2; both of which are located on the same part.

Equations (15) and (16) together with a proportional gain can be used in a resolved rate control scheme [2] to control the position and orientation of the part as shown in the next section.

4. Off-line Assembly Planning

In this section, we show how a synthetic image can be used to test image processing routines and to generate reference image features for control. Much of our work has concentrated on developing an optics simulator and off-line image processing extractor which is used to generate an augmented assembly plan. In Figure 11, the bold boxes represent computer programs which process the data files in the remaining boxes. The off-line system reads in the task plan from one file and the boundary representation of the CAD part from the ".dxf" file. A

synthetic image is generated using the Fourier Optics from which a variety of image processing routines are tested and image features are automatically selected for control [19].
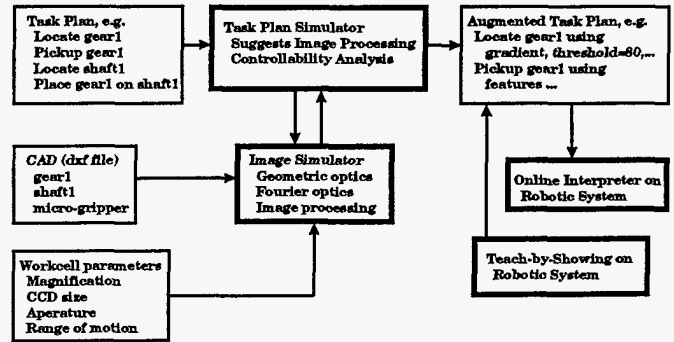

Figure 11. Block Diagram of CAD to Assembly Process.

To date, we have successfully tested using a synthetic image to visually servo a LIGA gear to a desired x,y position. Figures 12-14 show a sequence of images as the gear on the stage is visually servoed to the reference image position. Figure 12 shows the synthetic image which was generated from the CAD information. The part was recognized and located by finding the center of the part and then searching for 18 gear teeth on the outer diameter and a notch on the inner diameter. Its location in the image serves as the reference position. Figure 13 shows a real part as seen by the microscope and the application of the same image processing routines to locate the gear. Next, the part is visually servoed to the reference position at 30 Hz using the x,y centroid of the gear. Figure 14 shows the final position of the gear after visual servoing. Currently, the repeatability of the visual servoing is 1 micron in the x and y directions.

5. Conclusion

This paper described a prototype micromanipulation workcell for assembly of LIGA parts. We have demonstrated the ability to visually servo the LIGA parts to a desired *x,y* position between the tweezers. Fourier optics methods were used to generate a synthetic image from a CAD model. This synthetic image was used to select image processing routines and generate reference features for visual servoing. In the near future, we plan to generate a sequence of synthetic images which represent assembly steps, e.g. tweezer grasps gear, locate shaft, and put gear on shaft. Again, these images will be used to select image processing routines and generate reference features for visual servoing.
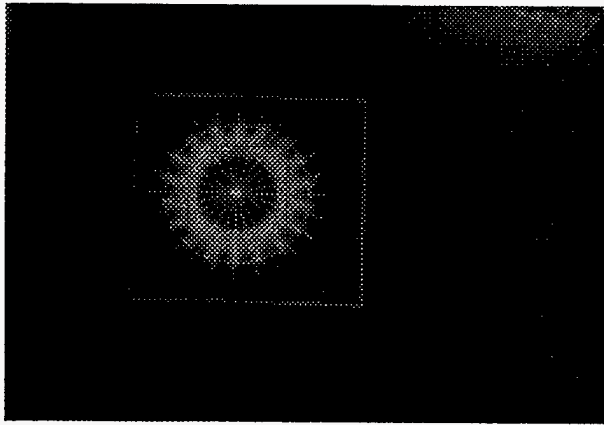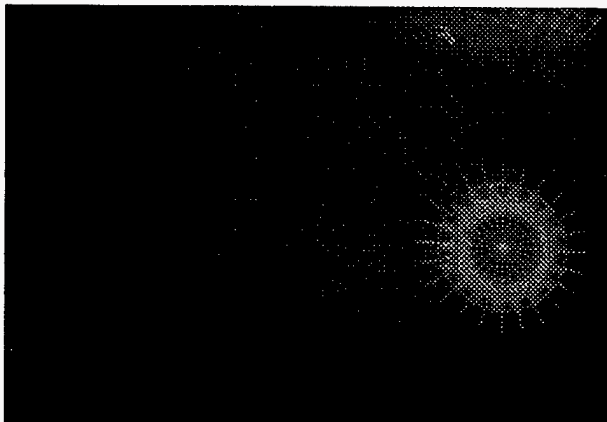
Figure 12. Synthetic reference image.

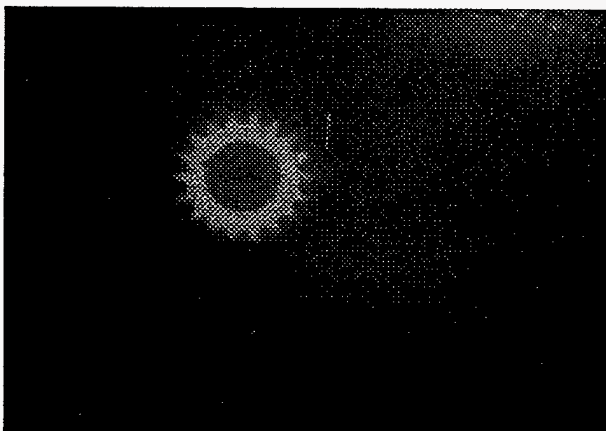*Figure 13. Initial location of real gear.*

Figure 14. Final position after visual servoing.

References

[1] P.I. Corke, "Visual Control of Robot Manipulators - A Review,"*Visual Servoing: Real-Time Control of Robot Manipulators Based on Visual Sensory Feedback*, Ed. K. Hashimoto, World Scientific Publishing Co. Pte. Ltd., Singapore, 1993.

[2] S. Hutchinson, G.D. Hagar, P.I. Corke, "A Tutorial on Visual Servo Control," *IEEE Trans. On Robotics and Automation*, Vol. 12, No. 5, pp. 651-670, Oct. 1996.

[3] R. Arai, D. Ando, T. Fukuda, Y. Nonoda, T. Oota, "Micro Manipulation Based on Micro Physics - Strategy Based on Attractive Force Reduction and Stress Measurement," *Proc. of ICRA 1995*, pp. 236-241.

[4] R.S. Fearing, "Survey of Sticking Effects for Micro Parts Handling," *Proc. of IROS '95*, Pittsburgh, PA, August 1995, Vol. 2, pp. 212-217.

[5] H. Miyazaki, T. Sato, "Pick and Place Shape Forming of Three-Dimensional Micro Structures from Fine Particles," *Proc. of ICRA 1996*, pp. 2535-2540.

[6] K. Koyano, T. Sato, "Micro Object handling System with Concentrated Visual Fields and New Handling Skills," *Proc. of ICRA 1996*, pp. 2541-2548.

[7] M. Mitsuishi, N. Sugita, T. Nagao, Y. Hatamura, "A Tele-Micro Machining System with Operation Environment Transmission under a Stereo-SEM," *Proc. of ICRA 1996*, pp. 2194-2201.

[8] W. Zesch, M. Brunner, A. Weber, "Vacuum Tool for Handling Microobjects with a Nanorobot," *Proc. of ICRA 1997*, pp. 1761-1766.

[9] A. Sulzmann, H.-M. Breguett, J. Jacot, "Microvision system (MVS): a 3D Computer Graphic-Based Microrobt telemanipulation and Position Feedback by Vision," *Proc. of SPIE Vol. 2593*, Philadelphia, Oct. 25, 1995.

[10] B. Vikramaditya and B. J. Nelson, "Visually Guided Microassembly using Optical Microscope and Active Vision Techniques," *Proc. of ICRA 1997*, pp. 3172-3178.

[11] A.P. Pentland, "A New Sense of Depth of Field," *IEEE Trans. on PAMI*, Vol. PAMI-9, No. 4, July 1987.

[12] J. Ens and P. Lawrence, "An Investigation of Methods for Determining Depth of Focus," *IEEE Trans. on PAMI*, Vol. 15, No. 2, February 1993.

[13] S.K. Nayar and Y. Nakagawa, "Shape from Focus," *IEEE Trans. on PAMI*, Vol. 16, No. 8, August 1994.

[14] M. Subbarao and T.Choi, "Accurate Recovery of Three-Dimensional Shape from Image Focus," *IEEE Trans. on PAMI*, Vol. 17, No. 3, March 1995.

[15] J. Feddema, M. Polosky, T. Christenson, B. Spletzer, R. Simon, "Micro-Grippers for Assembly of LIGA Parts," *Proc. of World Automation Congress '98*, Anchorage, Alaska, May 10-14, 1998.

[16] M. Bass, *Handbook of Optics*, 2nd Edition, Vol. II, pp. 17.1-17.52, McGraw-Hill, 1995.

[17] L.C. Martin, *The Theory of the Microscope*, American Elsevier Publishing Company, 1966.

[18] G.O. Reynolds, J.B. DeVelis, G.B. Parret, B.J. Thompson, *The New Physical Optics Notebook: Tutorials in Fourier Optics*, SPIE, 1989.

[19] J.T. Feddema, C.S.G. Lee, and O.R. Mitchell, "Weighted Selection of Image Features for Resolved Rate Visual Feedback Control," *IEEE Trans. On Robotics and Automation*, Vol. 7, pp. 31-47, Feb. 1991.

Report Number (14) _SAND--98-0621C_
CONF-980537--

Publ. Date (11) _19980310_
Sponsor Code (18) _DOE/CR, XF_
UC Category (19) _UC-900, DOE/ER_

DOE